Volume 1
Number 2
March 2023
Pages 97–172

# EES Catalysis

rsc.li/EESCatalysis

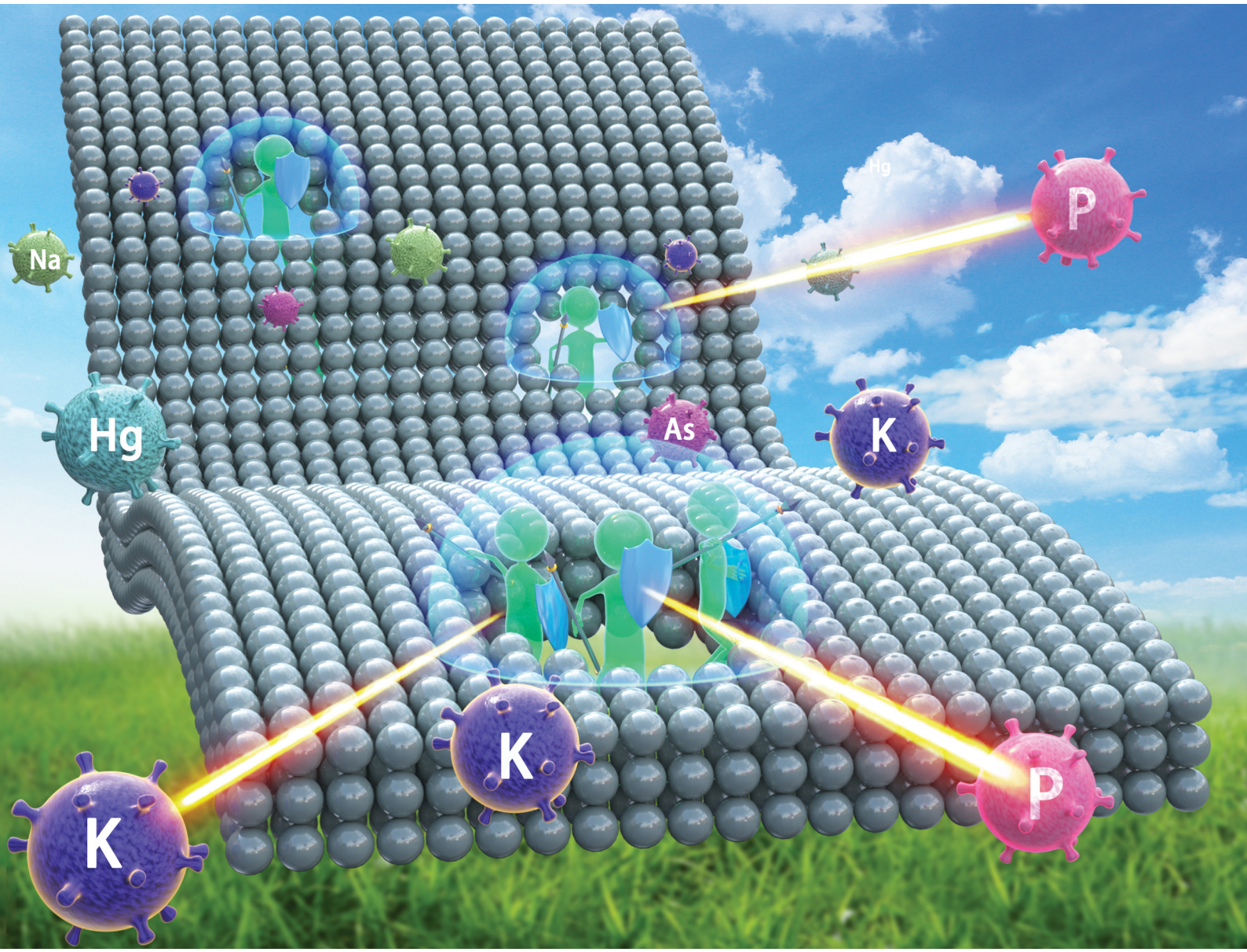


ISSN 2753-801X

ROYAL SOCIETY OF CHEMISTRY

**PAPER**

Baodong Wang, Ziran Ma, Yujie Xiong, Yun Wang *et al.*
An anti-poisoning defective catalyst without metal active sites for $NH_3$-SCR *via in situ* stabilization

EES Catalysis

PAPER

View Article Online
View Journal | View Issue



Cite this: *EES Catal.*, 2023, **1**, 134

# An anti-poisoning defective catalyst without metal active sites for $NH_3$-SCR *via in situ* stabilization†

Ge Li,[a] Baodong Wang,*[ab] Ziran Ma,*[a] Jing Ma,[a] Hongyan Wang,[a] Jiali Zhou,[a] Shengpan Peng,[a] Jessica Jein White,[c] Yonglong Li,[a] Jingyun Chen,[a] Zhihua Han,[a] Hui Wei,[a] Chuang Peng,[d] Yujie Xiong*[e] and Yun Wang*[c]

Received 25th October 2022,
Accepted 16th January 2023

DOI: 10.1039/d2ey00077f

rsc.li/eescatalysis

$NO_x$ emission can be controlled through selective catalytic reduction (SCR) by ammonia in industry. However, the SCR catalysts are sensitive to contaminants. Searching for anti-poisoning catalysts has become a perpetual quest for large-scale SCR. Here, we report that hydrogenated titanium dioxide particles containing oxygen vacancies undergo *in situ* N-doping during $NH_3$-SCR reaction. The N-doped hydrogenated $TiO_{2-x}$ exhibits high denitrification activity and selectivity, long-term stability, $H_2O$ and $SO_2$ tolerance, and high poisoning resistance. The DRIFT spectra combined with density functional theory computations demonstrate that the N-dopant as the catalytic active site can enhance $O_2$ and NO adsorption, which can be reduced by $NH_3$ *via* the Eley–Rideal mechanism. This is greatly different from traditional catalysts with metal active sites for $NH_3$ adsorption. The high anti-poisoning performance can be ascribed to the weak interaction between N and toxic reactants. This discovery creates a new concept that non-metal active sites can replace conventional precious/transition metals to avoid poisoning, while being stabilized by *in situ* doping with reactants.



**Broader context**

$NO_x$ emission can be controlled through selective catalytic reduction (SCR) by ammonia in industry. However, the SCR catalysts are sensitive to contaminants. Searching for anti-poisoning catalysts has become a perpetual quest for large-scale SCR. We report that hydrogenated titanium dioxide particles containing oxygen vacancies undergo *in situ* N doping during $NH_3$-SCR reaction. The N-doped hydrogenated $TiO_{2-x}$ exhibits high denitrification activity and selectivity, long-term stability, $H_2O$ and $SO_2$ tolerance, and high poisoning resistance. The DRIFT spectra combined with density functional theory computations demonstrate that the N-dopant as the catalytic active site can enhance $O_2$ and NO adsorption, which can be reduced by $NH_3$ *via* the Eley–Rideal mechanism. This is greatly different from traditional catalysts with metal active sites for $NH_3$ adsorption. The high anti-poisoning performance can be ascribed to the weak interaction between N and toxic reactants. This discovery creates a new concept that non-metal active sites can replace conventional precious/transition metals. Moreover, the results of this work provide a better understanding of the role of defect engineering for the design of highly poison-resistant, stable catalysts for a wide variety of reactions.

## Introduction

Nitrogen oxides ($NO_x$) are one of the main air pollutants, and the source of acid rain, ozone, photochemical smog, regional ultrafine particle (PM2.5) and haze, which affect human health and sustainable economic development. Selective catalytic reduction (SCR) is the most efficient and mature denitrification technology in stationary and mobile sources. Its success is determined by the development of $NH_3$-SCR catalysts with high activity, selectivity and long-term stability. The active components are often made of precious/transition metals that account for 50–70% of the total cost of the catalyst. Moreover, in the real denitrification process, alkali/alkaline metals (Na, K, Ca *etc.*), heavy metals (As, Pd, *etc.*), P, $SO_2$ and water vapor could deactivate the catalysts severely. These poisons can block,

[a] *National Institute of Clean-and-Low-Carbon Energy, Beijing 102211, China. E-mail: baodong.wang.d@chnenergy.com.cn, ziran.ma@chnenergy.com.cn*
[b] *NICE Europe Research GmbH, Stockholmer Platz 1, Stuttgart 70173, Germany*
[c] *Centre for Catalysis and Clean Energy, School of Environment and Science, Gold Coast Campus, Griffith University, Queensland 4222, Australia. E-mail: yun.wang@griffith.edu.au*
[d] *School of Resource and Environmental Sciences and Hubei International Scientific and Technological Cooperation Base of Sustainable Resource and Energy, Wuhan University, Wuhan 430072, China*
[e] *School of Chemistry and Materials Science, University of Science and Technology of China, Hefei, Anhui 230026, China. E-mail: yjxiong@ustc.edu.cn*

† Electronic supplementary information (ESI) available. See DOI: https://doi.org/10.1039/d2ey00077f

directly combine with or react with the active components of the catalysts, leading to limited useable lifespan of the catalysts and high economic cost due to frequent catalyst replacement.[1–6] To this end, the anti-poisoning performance of denitrification catalysts is not only an important indicator affecting the cost of the catalysts, but also an aspect of the sustainable development of $NH_3$-SCR.

Various additives including sacrificial agents or acidic/basic additives have been used to modify the denitrification catalyst support structures. Other approaches have involved controlling the catalyst synthesis to tune the crystalline structure, morphology, distribution of active components and interaction of the metal with the support to improve the anti-poisoning characteristics.[2–6] However, these methods only reduce poisoning agents without completely eliminating them. Therefore, the development of low-cost, poisoning-resistant denitrification catalysts is an ultimate goal. One promising strategy for the design of anti-poisoning catalysts is through defect engineering.[7–25] The distortion of the crystal structure can modify the Fermi energy level to promote the electron transitions necessary for the catalytic effect.[7–9] In addition, the defects can act as the active components for reactant adsorption, facilitate electron interaction and transfer, and reduce intrinsically wide band gaps. More importantly, the precious/transition metals are no longer required to act as active components because the defects can act as the active sites with unsaturated coordination numbers. As such, the poisoning of precious/transition metals would be mitigated, while the expense of the catalysts can be greatly reduced. However, some defects are very unstable, forming a major obstacle for practical applications. For example, the oxygen vacancies can be re-oxidized during prolonged storage in the atmosphere.[26–29] Therefore, such oxygen vacancy-based catalysts need to be stored in isolation from oxygen, which increases the cost and restricts industrial applications. To address this issue, it is desirable to design poison-resistant defective catalysts with outstanding stability, but this is challenging.

Here, we demonstrated that the defect sites designated for $NH_3$-SCR reaction can be stabilized by their interaction with reactants ($NH_3$ and NO), overcoming the dilemma between catalyst activity and stability. To eliminate the use of precious/transition metals, oxygen vacancies were created in $TiO_2$ crystals using a hydrogenation method. The hydrogenated $TiO_{2-x}$ (H-$TiO_{2-x}$) was used as a catalyst for the $NH_3$-SCR, which leads to *in situ* N-doping on the defective H-$TiO_{2-x}$ catalyst (N-H-$TiO_{2-x}$). Our results reveal that N-H-$TiO_{2-x}$ exhibits superior denitrification activity. More importantly, it has long-term stability because of its tolerance of $H_2O$ and $SO_2$ and significant poisoning resistance, such as $SO_2$, $H_2O$, P, and alkali metals. The results of this work provide a better understanding of the role of defect engineering for the design of highly poison-resistant, stable catalysts for a wide variety of reactions.

## Results and discussion

### $NH_3$-SCR performance of the hydrogenated $TiO_{2-x}$ catalyst

Fig. 1 shows the $NH_3$-SCR activity of the H-$TiO_{2-x}$ catalyst compared with those of pristine $TiO_2$ and commercial VW/Ti

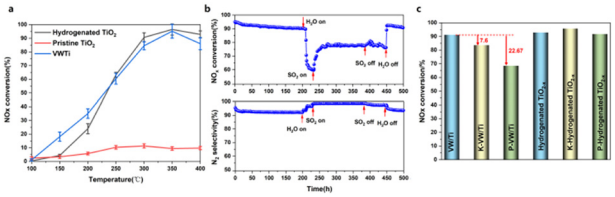


Fig. 1 $NH_3$-SCR denitrification activity of the catalyst. (a) The denitrification performances of pristine $TiO_2$, H-$TiO_{2-x}$ and VW/Ti catalysts. (b) Data from 500 h durability trials with the H-$TiO_{2-x}$ catalyst at 350 °C. (c) Tolerance of $K_2O$ and $P_2O_5$ of the H-$TiO_{2-x}$ catalyst and of commercial VW/Ti catalysts at 350 °C.

catalysts. From Fig. 1a the denitrification efficiency of the pristine $TiO_2$ was only 7.3–12.8% at 250–400 °C. However, following hydrogenation, the denitrification activity was dramatically increased, to more than 90% at 300–400 °C, representing an increase of approximately 80%, almost reaching the efficiency of the commercial VW/Ti catalyst. The selectivity for $N_2$ was essentially unchanged after hydrogenation, remaining above 87.5% (Fig. S1, ESI†). The stability and resistance to $H_2O$, $SO_2$, $K_2O$ and $P_2O_5$ of the H-$TiO_{2-x}$ catalyst were also tested. As shown in Fig. 1b, a 500 h stability test was carried out to investigate the stability of the catalyst at 350 °C. The denitrification efficiency was found to slightly decrease by 4.86%, while the $N_2$ selectivity dropped by only 3.29% for 200 h with $NH_3$, NO and $O_2$ blowing in. The resistance of the H-$TiO_{2-x}$ catalyst to $H_2O$ and $SO_2$ at 350 °C is followed, conducted as shown in Fig. 1b, which indicates that the denitrification efficiency dropped sharply (by 31.3%) after 8% $H_2O$ was introduced into the reaction system for 30 h. Water molecules are believed to have covered the oxygen vacancies on the surface of the catalyst or to have competed with NO and/or $NH_3$ for adsorption on the catalyst surface, resulting in a decrease in denitrification activity. Interestingly, when 800 ppm $SO_2$ was also introduced into the reaction system, the denitrification activity slowly increased and was maintained at 77–79% for 220 h. These results demonstrate that hydrogenated $TiO_{2-x}$ showed good water and sulfur resistance and suitable long-term stability. The trial using 8% $H_2O$ and 800 ppm $SO_2$ at 350 °C provided a $N_2$ selectivity of greater than 98% (Fig. 1b). This performance can possibly be ascribed to the formation of more acidic sites on the surface of the catalyst following the introduction of $SO_2$, leading to an increase in the activity and the $N_2$ selectivity.[30,31] When the supply of $SO_2$ was cut off, the $NO_x$ conversion remained relatively constant, while after the $H_2O$ flow was stopped, the $NO_x$ conversion increased sharply and returned to its initial level. These results establish that the effects of water on the catalyst were reversible. To better evaluate the anti-poisoning performance of the hydrogenated $TiO_{2-x}$ catalyst, a conventional SCR catalyst (1V8W/$TiO_2$) was prepared for comparison and simulated poisoning experiments were conducted using an impregnation method. Fig. 1c demonstrates that, under the same temperature and reaction conditions, the denitrification activity of the 1V8W/$TiO_2$ catalyst was decreased by 7.6% and 22.67% with K and P poisoning, respectively.

Surprisingly, the performances of the hydrogenated $TiO_{2-x}$ catalysts poisoned by K and P were almost unchanged.

### Reaction mechanism

The HRTEM and XRD results shown in Fig. S2 and S3 (ESI†) demonstrated that the phase composition of the H-$TiO_{2-x}$ was primarily anatase. The Raman, EPR, $^1$H NMR and photoluminescence spectra combined with the $O_2$-TPD and $H_2$-TPD shown in Fig. S4–S9 (ESI†) further demonstrate the existence of oxygen vacancies. The *in situ* X-ray photoelectron spectroscopy (XPS; Fig. S10–S12, ESI†) results confirm that oxygen vacancies and $Ti^{3+}/Ti^{4+}$ were produced on the surface of the H-$TiO_{2-x}$ catalyst. The *in situ* XPS data obtained during the $NH_3$-SCR reaction are presented in Fig. 2 and Fig. S13–S15 (ESI†). Fig. 2a presents the N 1s spectra of the material. The spectra obtained over the range of 150–400 °C each contain a O–Ti–N peak related to interstitial doping at approximately 399 eV. The transition from a mixture of $Ti^{3+}$ and $Ti^{4+}$ to solely $Ti^{4+}$ after N-doping is shown in Fig. S14 (ESI†). Because the electronegativity and radius of the N ions (3.04 and 0.171 nm, respectively) are similar to those of O ions (3.44 and 0.140 nm, respectively), N-doping of the H-$TiO_{2-x}$ crystal lattice is expected. The N-doping into the H-$TiO_{2-x}$ catalyst might have come from $NH_3$ or $NO_x$ in the reaction gas. Thus, XPS spectra were obtained from the H-$TiO_{2-x}$ after trials in which only $NH_3$ or NO + $O_2$ were present. Fig. S16 (ESI†) demonstrates that N-doping of the H-$TiO_{2-x}$ catalyst surface occurred under both conditions. Previous studies have shown that the nitrogen-doping of $TiO_2$ can proceed under an $NH_3$ atmosphere at 500 °C as N from $NH_3$ partially replaces the lattice oxygen of $TiO_2$, forming O–Ti–N and oxygen vacancies. The present hydrogenation process generated oxygen vacancies in the $TiO_2$ in advance, making nitrogen-doping more likely to occur at lower temperatures (150–400 °C), which is a unique phenomenon in the de$NO_x$ reaction. Based on the NIST database,[32] the peaks near 406–407 eV were attributed to N–H bonds in $NH_4NO_3$. As shown in Fig. 2b, the N–H peak gradually decreased with increasing temperature, while the O–Ti–N peak gradually increased, suggesting that elevated temperature promotes N-doping. Comparing these data to the results shown in Fig. 1a demonstrates that the degree of N-doping was proportional to the denitrification activity. The results from 200 h stability trials with only $NH_3$, NO and $O_2$ blowing in indicated that *in situ* N-doping improved the stability of the catalyst.

The local atomic structure and cation coordination in the catalyst before and after N-doping were ascertained using XAFS (Fig. 3). The Ti K-edge X-ray absorption near-edge structure (XANES) spectra of hydrogenated $TiO_{2-x}$ and the N-hydrogenated $TiO_{2-x}$ catalyst possessed three typical pre-edge peaks associated with the anatase phase (denoted as A1, A2, and A3 at 4968, 4971, and 4974 eV, respectively), corresponding to quadruple-allowed 1s to 3d transitions.[19] Furthermore, it has recently been suggested that most of the contribution to pre-edge splitting is from the edge and corner sharing of Ti ions in the $TiO_6$ octahedra with oxygen ions, which lead to non-local, intersite hybrid excitations. Therefore, the variation in pre-edge peak area during sample

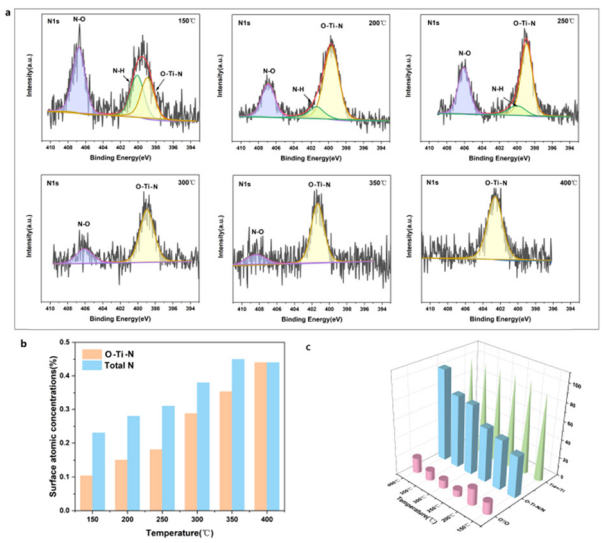


Fig. 2 The *in situ* XPS spectra obtained from the H-$TiO_{2-x}$ during the $NH_3$-SCR process at 150–400 °C. (a) N1s. (b) Surface N atom concentrations and O–Ti–N concentrations at various temperatures. (c) Percentage content of the active components O, N and Ti (O′ = $O_\beta$ + $O_\gamma$).

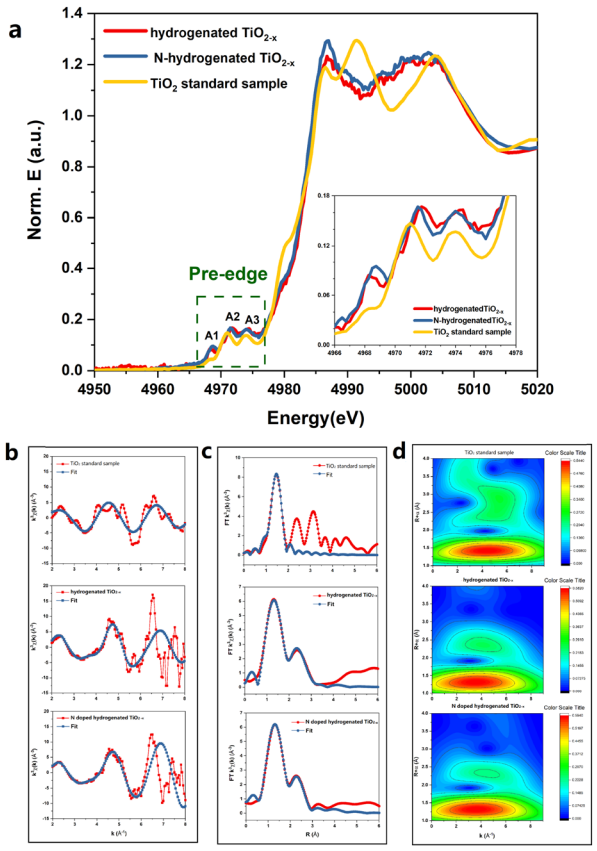


Fig. 3 The XANES spectra of the catalyst samples before and after the SCR reaction. (a) The Ti K-edge, (b) extended region fitting using ARTEMIS in R-space, (c) fitted magnitude of $k_3$-weighted Ti K-edge EXAFS spectra, and (d) wavelet transform images obtained for the $TiO_2$ standard sample (anatase), hydrogenated $TiO_{2-x}$ and N-hydrogenated $TiO_{2-x}$.

etching can be interpreted as the change in the Ti 3d unoccupied states due to the interaction of Ti 4p, O 2p, and Ti 3d states. The total area of the pre-peaks was associated with the number of unoccupied next-nearest-neighbour Ti 3d states. As clearly shown in Fig. 3, for both hydrogenated $TiO_{2-x}$ and the N-hydrogenated $TiO_{2-x}$ catalyst, the area of the near-side peaks was significantly larger than that of the $TiO_2$ standard sample (anatase), which was due to oxygen vacancies. For the hydrogenated $TiO_{2-x}$ catalyst and *N*-hydrogenated $TiO_{2-x}$ catalyst, the A1, A2, and A3 peaks were all observed to shift to a higher energy compared with the $TiO_2$ standard sample (anatase). This was attributed to the higher oxidation state of the core metal atom (Ti), as induced by oxygen vacancies in the coordination sphere. The intensity of the A2 peak increased with increasing site distortion in the order $TiO_2$ < hydrogenated $TiO_{2-x}$ ≈ *N*-hydrogenated $TiO_{2-x}$. The introduction of oxygen vacancies made the crystal lattice more disordered. From Fig. 3a, after N-doping, the A2 peak of the catalyst was shifted to a slightly lower energy, supporting that nitrogen filled the oxygen vacancies. Fig. 3b and c show the EXAFS oscillations for the standard, hydrogenated and *N*-hydrogenated $TiO_{2-x}$, respectively. Fig. 3d clearly demonstrates that the Ti–O coordination environment was only minimally changed after N-doping, while the Ti–Ti coordination environment changed greatly. These changes confirm the transition from a mixture of $Ti^{3+}$ and $Ti^{4+}$ to solely $Ti^{4+}$ after N-doping.

The distributions of formal valences in the catalyst before and after N-doping were probed using EELS-STEM, while simultaneously acquiring Ti–L, N–K and O–K edge data (Fig. 4). The Ti–L edge provided a fingerprint of the $Ti^{4+}$ and $Ti^{3+}$ states and the O–K edge was sensitive to the presence of oxygen vacancies. In the case of the H-$TiO_{2-x}$ catalyst, the EELS spectra were collected close to (0.9, 1.8, 2.7 and 3.6 nm) and far from (6.3 nm) the interface and the results are presented in Fig. 4a. These data indicate that the Ti-L2 peak was shifted by 0.6 eV from the crystalline side to the amorphous side, demonstrating the presence of $Ti^{3+}$ in the amorphous layer, at the interface and on the crystalline side close to the interface (within 2.7 nm). In Fig. 4b, the N–K peak appeared at 0.9 nm, showing that the surface nitrogen-doping occurred primarily in the amorphous layer. Furthermore, no Ti–L peak shifts were observed, further demonstrating that $Ti^{4+}$ was the primary state in the *N*-hydrogenated $TiO_{2-x}$.

Fig. 5 and Fig. S17 (ESI†) provide the *in situ* infrared spectra of H-$TiO_{2-x}$ and pristine $TiO_2$. These data indicate that very little NO or $O_2$ was adsorbed on the pristine $TiO_2$ (Fig. 5a), while bridged bidentate nitrate (at 1610 $cm^{-1}$), chelated bidentate nitrate (1578 and 1238 $cm^{-1}$) and monodentate nitrite (1350 $cm^{-1}$)[30] were formed on the hydrogenated $TiO_{2-x}$. These results are in agreement with the poor denitrification activity of this material. This difference is attributed to the abundant oxygen vacancies present on the H-$TiO_{2-x}$ surface, which are able to oxidize NO to $NO_2$ and generate a series of nitrates and nitrites. Exposure to $NH_3$ did not modify the surface of the pristine $TiO_2$ although the chelated bidentate nitrate on the H-$TiO_{2-x}$ disappeared and no $NH_3$ adsorption peak was obtained, indicating that gaseous $NH_3$ reacted with nitrate on the catalyst surface. Following the surface adsorption of $NH_3$ (Fig. 5b), the pristine $TiO_2$ generated an $NH_3$ adsorption peak at the L acid position at 1103 $cm^{-1}$. The results obtained from $NH_3$-temperature programmed desorption (Fig. S18, ESI†) and pyridine adsorption infrared spectroscopy (Fig. S19, ESI†) show that the pristine $TiO_2$ was somewhat acidic and was also able to adsorb $NH_3$. In contrast, the surface adsorption of $NH_3$ on the H-$TiO_{2-x}$ generated $NH_4^+$ at B acid sites (1633 $cm^{-1}$) together with $NH_2$ (1322 and 1492 $cm^{-1}$) and $NH_3$ at L acid sites (1197 $cm^{-1}$). Exposure to NO and $O_2$ had little effect on the surface of the pristine $TiO_2$. However, the

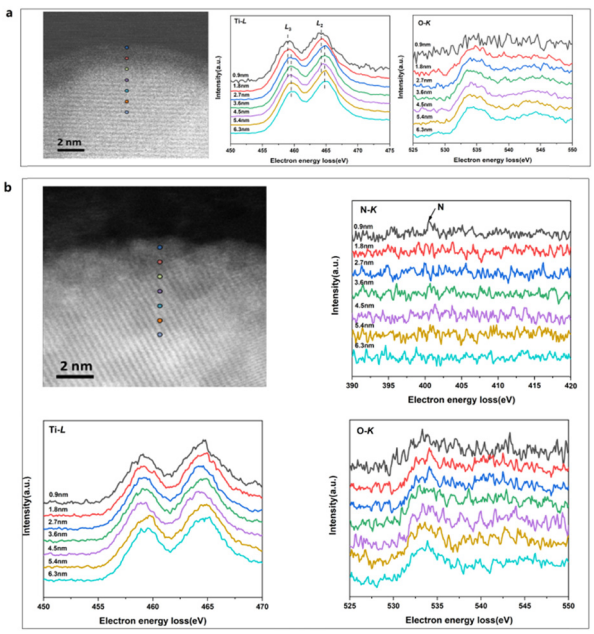


Fig. 4 The EELS-STEM spectra of the catalysts. (a) The H-$TiO_{2-x}$ catalyst and (b) the N-H-$TiO_{2-x}$ catalyst.

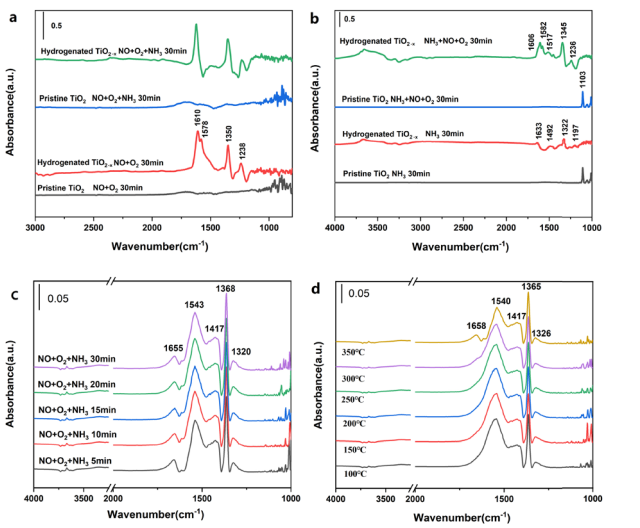


Fig. 5 The DRIFT spectra obtained from the hydrogenated $TiO_{2-x}$ and pristine $TiO_2$. (a) NO and $O_2$ followed by $NH_3$ at 300 °C. (b) $NH_3$ followed by NO + $O_2$ at 300 °C. (c) $NH_3$ + NO + $O_2$ for 30 min at 300 °C. (d) $NH_3$ + NO + $O_2$ with a temperature gradient.

H-$TiO_{2-x}$ formed bridged bidentate nitrate (1606 $cm^{-1}$), chelated bidentate nitrate (1578 and 1236 $cm^{-1}$), monodentate nitrite (1517 $cm^{-1}$) and ammonium nitrate (1346 $cm^{-1}$). The $NH_3$ adsorption peaks at L acid and B acid sites also disappeared, indicating that $NO_x$ had reacted with adsorbed $NH_3$. These results confirmed that the adsorption of $NH_3$ and gaseous $NO_x$ proceeded according to the Eley–Rideal mechanism.[33–35]

Fig. 5c shows the *in situ* infrared spectra obtained from the N-H-$TiO_{2-x}$ catalyst at 300 °C following a simultaneous exposure to NO, $O_2$ and $NH_3$. When the three gases were introduced for 5 min, peaks related to bridged bidentate nitrate (1655 $cm^{-1}$), monodentate nitrate (1543 $cm^{-1}$) and monodentate nitrite (1368, and 1320 $cm^{-1}$) appeared.[36] With prolonged exposure to the three gases simultaneously, the intensity of these peaks changed only minimally, indicating that these compounds were stable on the catalyst surface. No $NH_3$ adsorption peak was observed, which suggests that $NH_3$ is the primary participant in the gas phase $NH_3$-SCR reaction. Fig. 5d provides the steady state *in situ* infrared spectra acquired from the N-H-$TiO_{2-x}$ catalyst surface at different temperatures in conjunction with the simultaneous introduction of $NH_3$, NO and $O_2$ during the SCR reaction. At 100 °C, a series of peaks attributed to $NO_x$ species adsorbed on the catalyst surface appeared. The peaks at 1658 and 1540 $cm^{-1}$ represent bridged and chelated bidentate nitrates, respectively, while those at 1365 and 1326 $cm^{-1}$ indicate monodentate nitrite. As the temperature was gradually increased, the intensity of the chelated bidentate nitrate peak decreased significantly, due to desorption from the catalyst surface. Again, peaks related to the adsorbed $NH_3$ were not observed. It is apparent that $NH_3$ and chelated bidentate nitrate were active on the catalyst surface and participated in the SCR reaction through the Eley–Rideal mechanism. We will carry out kinetic experiments in the subsequent research and quantify the proportion of E–R mechanism according to the kinetic calculation. It is worthy of note that the assignment of the band at 1417 $cm^{-1}$ still needed further identification. The peaks in some studies[37–40] are close to 1417 $cm^{-1}$, but their attribution of this peak is various. Moreover, we have not found literature with exactly the same peak as ours. This may be because other studies are all on catalysts with metal active sites and the functional groups on the catalyst surface are different from those of our catalysts without metal active sites. The peak of 1417 $cm^{-1}$ in the *in situ* infrared spectrum is unique to our catalyst. As such, the ascription of the strong IR absorption peak at 1417 $cm^{-1}$ could be based on other characterizations and DFT simulation in our subsequent research.

## DFT calculations

Density functional theory (DFT) calculations were performed to better understand the role of lattice defects in the catalytic process.[37–39] The adsorption properties of specific small molecules on the pristine $TiO_2$ (101), H-$TiO_{2-x}$, and N-H-$TiO_{2-x}$ surfaces are presented in Fig. 6a–c. The Raman, EPR, $^1H$ NMR and photoluminescence spectra combined with the $O_2$-TPD and $H_2$-TPD shown in Fig. S4–S9 (ESI†) demonstrate the existence of oxygen vacancies in H-$TiO_{2-x}$. As a result, one surface oxygen vacancy was introduced here to model H-$TiO_{2-x}$. The oxygen vacancy was highlighted by a blue circle shown in Fig. 6b. The adsorption energies indicate that the pristine $TiO_2$ has a weak interaction with $O_2$ and NO. As a comparison, the adsorption of $NH_3$ on this surface was stronger. The surface $Ti^{4+}$ as L acid sites can adsorb a significant quantity of $NH_3$. On H-$TiO_{2-x}$, the $O_2$ and NO can tightly bind with the vacancy. $NH_3$ can still adsorb on L acid sites with an enhanced interaction strength. The adsorption energies of reactants match the $NH_3$-TPD and Py-IR spectra shown in Fig. S18 and S19 (ESI†). However, the strong adsorption of NO and $NH_3$ disagrees with DRIFT data with the Eley–Rideal mechanism because $NH_3$ needs to directly interact with the adsorbed reactants. This indicates that the oxygen vacancy is not the active site during the reactions. Interestingly, the NO and $O_2$ can tightly adsorb through the interaction with the N-dopant after *in situ* N-doping. This indicates that the surface N-dopant can act as the catalytic active site. In particular, the NO adsorption energy on N *via* a N–N–O configuration is −2.88 eV (see Fig. 6c), which is 1.04 and 1.80 eV lower than those of $O_2$ and $NH_3$. The formation of a N–N bond weakens the N–O bond in NO, as evidenced by the enlarged N–O bond length from 1.17 in NO gas to 1.32 Å after adsorption. More importantly, the $NH_3$ can dissociatively adsorb on the pre-adsorbed NO to form *OH and *N–$NH_2$ as shown in Fig. 6d. The dissociative adsorption of $NH_3$ on the –N–N–O site is because N in NO carries a positive charge and, therefore unoccupied orbitals. On the other hand, the N in $NH_3$ has lone-pair electrons. As a result, the N in $NH_3$ can strongly

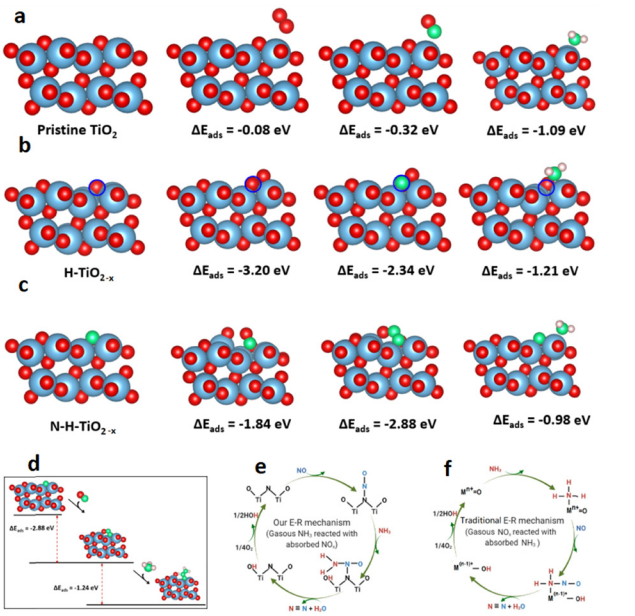


Fig. 6 (a) Adsorption of $O_2$, NO and $NH_3$ on pristine $TiO_2$ (101), (b) adsorption of $O_2$, NO and $NH_3$ on H-$TiO_{2-x}$, (c) adsorption of $O_2$, NO and $NH_3$ on N-H-$TiO_{2-x}$, (d) reaction coordinates of $NH_3$-SCR *via* the Eley–Rideal mechanism, (e) SCR reaction routes at the N active sites in the N-H-$TiO_{2-x}$ catalyst, and (f) SCR reaction routes at the metal active sites in the traditional catalysts. Legend: red = O; blue = Ti; pink = H; and green = N; blue circle = oxygen vacancy.

bind with N in adsorbed NO through dative covalent bonding. At the same time, the $NH_3$ was dissociated after the adsorption because of the strong O–H bonding between the negatively charged O in NO and positively charged H in $NH_3$. The adsorption energy is −1.24 eV, which is 26.5% lower than that of the direct adsorption of $NH_3$ on the $Ti^{4+}$ L acid site. Moreover, there is no steric effect in the interaction between $NH_3$ and NO. Consequently, the Eley–Rideal mechanism derived from the DRIFT spectra is supported by the DFT results. The novel SCR reaction route through the adsorption of NO on the N active sites in the N-H-$TiO_{2-x}$ catalyst is illustrated in Fig. 6e, which is compared with the mechanism through the adsorption of $NH_3$ on metal active sites in the traditional catalysts shown in Fig. 6f.

The DFT computations combined with *in situ* DRIFTS experiments were also used to explain the resistance of the N-H-$TiO_{2-x}$ catalyst to $H_2O$, $SO_2$ and K poisoning. Fig. 7a shows that the water can adsorb at the bridge site between surface $Ti^{4+}$ and N atoms on N-H-$TiO_{2-x}$ *via* hydrogen bonding. As a result, the N active sites can be blocked by adsorbed $H_2O$. This explains why the activity drops after the exposure of water, as shown in Fig. 1b. However, as the interaction strength of −0.87 eV is moderate *via* hydrogen bonding, the impact of $H_2O$ adsorption on the electronic properties of N-H-$TiO_{2-x}$ is limited. As such, the selectivity only changes slightly. After the further exposure of $SO_2$, the adsorbed water can interact with $SO_2$ and $O_2$ to form $H_2SO_4$.[40,41] The formation and desorption of $H_2SO_4$ is an exothermal process with the reaction energy of −1.32 eV. This indicates that the adsorbed water can be removed after the exposure of $SO_2$ and $O_2$, which can reactivate N active sites for denitrification, as shown in Fig. 1b, so that the activity of the N-H-$TiO_{2-x}$ catalysts recovers after the exposure of $SO_2$ to the catalyst with pre-adsorbed water. The DFT calculations also reveal that K atoms prefer not to adsorb on the oxygen vacancy, even when the K atom was initially placed at the vacancy site. The most stable configuration is shown in Fig. 7b. This is reasonable because the system becomes more stable when the K atom is bonded with more surface oxygen atoms. This means that the vacancy for the formation of active sites *via in situ* N-doping will not be poisoned by K. More interestingly, the NO adsorption can be strengthened when K is next to the N active site since K can extract O from NO, which leads to the formation of $N_2$ at the active site. This result explains why the denitrification efficiency increases slightly after K poisoning, as shown in Fig. 1c. When the metal acts as the active site in traditional $NH_3$-SCR catalysts, *e.g.*, VW/Ti, the metal as L acid sites can accommodate the lone pair electrons of O and S in toxic substances, which is the origin of the poisoning of these catalysts. Our results, therefore, demonstrate the unique anti-poisoning advantage of the non-metal active site for $NH_3$-SCR.

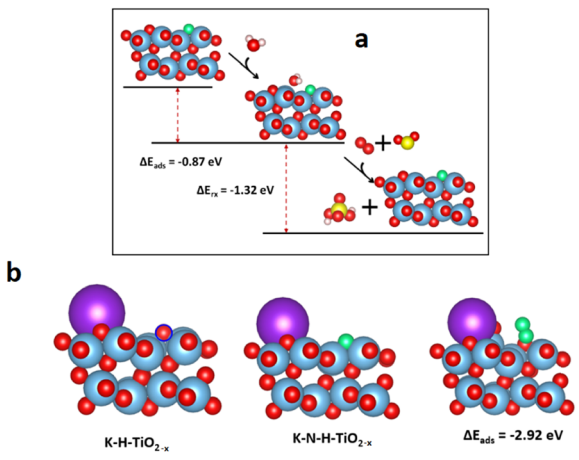


Fig. 7 (a) Reaction coordinates of adsorption of water followed by $SO_2$ on N-H-$TiO_{2-x}$, and (b) adsorption of K on H-$TiO_{2-x}$ and N-H-$TiO_{2-x}$ and NO adsorption on K–N-H-$TiO_{2-x}$. Legend: red = O; blue = Ti; pink = H; green = N; yellow = S; purple = K; and blue circle = oxygen vacancy.

## Experimental

### Synthesis of hydrogenated $TiO_{2-x}$ catalysts

Commercial titanium dioxide (Denox Advanced Material Co., Ltd in China, $TiO_2$ 97%, BET 323.36 $m^2\ g^{-1}$, rutile and anatase) powder was placed into a fixed bed reactor. Hydrogenated $TiO_{2-x}$ catalysts with $Ti^{3+}$ were prepared by a hydrogen thermal reduction treatment method by heating commercial titanium dioxide powders in 99.99% $H_2$ at 450 °C (heating rate 5 °C $min^{-1}$) under ambient pressure for 12 h. The $H_2$ flow velocity (100 mL $min^{-1}$) was controlled using a gas flow controller during hydrogen reduction treatment until cooling to room temperature. The hydrogenated $TiO_{2-x}$ powder is placed in a vacuum dryer to prevent the oxygen in the air from further oxidizing the catalyst. Hydrogenated $TiO_{2-x}$ powder was obtained as shown in eqn (1) and (2).

$$TiO_2 + xH_2(g) \rightarrow TiO_{2-x} + xH_2O(g) \quad (1)$$

$$O^{2-}(s) + H_2(g) \rightarrow H_2O(g) + V_O^{2-} \quad (2)$$

where $V_O^{2-}$ represents the oxygen vacancy.

A typical impregnation method was applied to prepare the alkali and P-poisoned catalysts. According to the literature, the mass ratios of K and P are 0.6 and 1 wt%, respectively. Therefore, 1 g of catalyst, 50 mL of deionized water, and a corresponding amount of KCl or/and $NH_4H_2PO_4$ were stirred together, dried, and calcined at 550 °C for 4 h in $N_2$. For comparison, commercial 1%V8%W/Ti catalyst poisoning was also prepared according to the above method. The poisoned samples were denoted as K-hydrogenated $TiO_{2-x}$, P-hydrogenated $TiO_{2-x}$, K-VW/Ti and P-VW/Ti.

### Characterization of the materials

X-Ray diffraction (XRD) was performed using a D8 ADVANCE diffractometer (Bruker, Germany), using Cu $K_\alpha$ radiation and a step size of 0.02°. Data were collected from 5° to 90° at a scanning rate of 3° $min^{-1}$.

High-resolution transmission electron microscopy (HRTEM) was performed using a JEOL JEM ARM200F instrument (Japan).

The electron paramagnetic resonance (EPR) spectra of the samples were acquired using a Bruker A320 instrument. The samples (0.12 g) were loaded into quartz tubes. EPR experiments of titanium dioxide powders and hydrogenated $TiO_{2-x}$ samples were conducted under normal temperature and pressure conditions. The reactor was placed in a heating furnace and heated to 500 °C at a heating rate of 10 °C $min^{-1}$ and pretreated with 2% $O_2$ for 1 h. After pretreatment, the gas supply was stopped and the reactor was sealed and cooled. Upon reaching room temperature, the EPR test was repeated. The magnetic field was swept from 1500 to 5000 G.

The Raman spectra were obtained using a LabRam HR-800 spectrometer (Horiba Jobin Yvon, France) with laser excitation at 532 nm.

X-Ray photoelectron spectroscopy (XPS) was performed using an ESCALAB 250xi instrument (Thermo Scientific, UK) using monochromatic Al $K_\alpha$ radiation (1486.6 eV) at 25 W. The samples were outgassed overnight at room temperature in an ultrahigh-vacuum chamber ($<5 \times 10^{-7}$ Pa). All binding energies were referenced to the C 1s peak at 284.6 eV. Experimental errors were within ±0.1 eV.

Solid-state NMR experiments were conducted on a Bruker Avance III HD/89 mm spectrometer with a 4 mm triple-resonance magic angle spinning probe.

$O_2$-temperature-programmed desorption (TPD) experiments were performed to determine the adsorption/desorption characteristics of each species over the catalyst. Each catalyst (200 mg) was loaded into the reactor, pretreated with $N_2$ (50 mL $min^{-1}$) at 100 °C for 30 min, and then cooled to room temperature in the same stream. The pretreated sample was then exposed to $O_2$ (3%) at a flow rate of 70 mL $min^{-1}$ for 30 min. Physisorbed $O_2$ was removed by flushing the catalyst with He at a flow rate of 30 mL $min^{-1}$ for 30 min at 120 °C prior to TPD. The samples were subjected to TPD in He (30 mL $min^{-1}$) from 100 to 600 °C at a heating rate of 10 °C $min^{-1}$.

$H_2$-temperature-programmed reduction (TPR) experiments were performed with an AutoChem II 2920 instrument (USA). The catalyst (0.3 g) was pretreated with Ar flow (50 mL $min^{-1}$) for 30 min at 500 °C to remove water and other impurities. As the samples cooled, the Ar flow was replaced with a reductive mixture of 10.0% $H_2$ in Ar and the reactor temperature was increased to 800 °C at a heating rate of 10 °C $min^{-1}$.

$NH_3$-TPD experiments were performed using an automatic physical and chemical adsorption instrument (AutoChem II 2920, Micromeritics). Before $NH_3$ adsorption at 373 K, the samples were heated at 773 K under He flow. The amount of $NH_3$ desorbed between 373 and 873 K at a heating rate of 10 K $min^{-1}$ was determined using an on-line gas chromatograph equipped with a thermal conductivity detector.

The diffuse reflectance infrared Fourier transform (DRIFT) spectra were recorded using an IR Prestige-21 instrument (Shimadzu) at a resolution of 4 $cm^{-1}$ and averaged over 500 scans. These experiments were performed by heating precalcined powder samples *in situ* from room temperature to 673 K at a heating rate of 5 K $min^{-1}$ under a pure $N_2$ flow (40 mL $min^{-1}$). The samples were kept at 673 K for 3 h and then cooled to 323 K. Pyridine vapor (20 μL) was then introduced under a $N_2$ flow. The IR spectra were recorded at various stages of pyridine desorption, which was maintained by evacuation at progressively higher temperatures (323–473 K). A resolution of 4 $cm^{-1}$ was achieved after averaging 500 scans for all the IR spectra recorded.

The *in situ* X-ray photoelectron spectroscopy (*in situ* XPS) measurements were conducted on a near ambient pressure (up to 2.5 kPa) X-ray photoelectron spectroscopy system (SPECS) equipped with a monochromatized Al Kα source ($h\nu$ = 1486.6 eV), gas atmosphere XPS analysis chamber (up to 2.5 kPa, 1000 K), electron analyzer (Phoibos 150), three-differential pumping stage that separates the analysis chamber from the electron energy analyzer, and sample preparation chamber (up to 3.0 MPa and 873 K). The X-ray source was set at an acceleration voltage of 15 kV and an irradiation power of 80 W. A preparation chamber was used for catalyst activation. Afterwards, the chamber was evacuated, and the sample was directly transferred into the analysis chamber under vacuum to avoid exposure to air. Firstly, the temperature was raised to 150 °C and then NO (1% NO, $N_2$, and 2 L $h^{-1}$) and $O_2$ (99.99%, 2 L $h^{-1}$) were blown in simultaneously. $NH_3$ (1% $NH_3$, $N_2$, and 2 L $h^{-1}$) is then introduced one hour later. After the catalyst adsorption equilibrium, the Ti spectra (including the valence band spectra), O spectra and N spectra of the catalyst at 150 °C, 200 °C, 250 °C, 300 °C, 350 °C and 400 °C were collected, respectively.

The distribution of Brønsted (B) and Lewis (L) acids on the synthesized catalyst was characterized using the pyridine infrared adsorption (Py-IR) method (IRPrestige-21, Shimadzu, Japan). Catalyst powder (20–30 mg) was weighed onto a sheet with a diameter of 13 mm, which was then fixed in an infrared cell. The temperature was increased to 500 °C for 60 min, then decreased to 350, 200, 100, and 30 °C, holding at each temperature for 5 min to measure the background value. Pyridine was adsorbed at 30 °C for 1 h, then purged for 30 min, and the adsorption spectrum was obtained. The temperature was then increased to 100, 200, and 350 °C, holding at each temperature for 5 min to measure the desorption spectra. The infrared spectra of the catalyst were recorded in the region of 1700–1400 $cm^{-1}$.

Photoluminescence spectroscopy (PL) was used to investigate oxygen vacancies on the catalyst surface (LabRam HR-800, Horiba Jobin Yvon, France). The light-induced spectral curve was measured at room temperature, and He–Cd was used as the laser source ($\lambda$ = 325 nm).

Thermogravimetric analysis, conducted on an STA 449 F3/QMS 403C instrument (Netzsch, Germany), was used to assess catalyst loss.

The catalyst electronic structure was determined using electron energy loss spectroscopy (EELS). The energy resolution of EELS with a monochromator was 0.15 eV measured at the full width at half-maximum of the zero-loss peak under vacuum, with the highest energy dispersion of 0.025 eV per channel. To obtain surface structures through direct observation of the atomic arrangement, an aberration-corrected dedicated FEI Titan Themis 60–300 instrument was used, achieving

atomic resolution (70 pm) in the high-angle annular dark-field imaging (HAADF) mode.

The X-ray absorption fine structure (XAFS) Ti K-edge spectra were collected at the BL07A1 beamline of the National Synchrotron Radiation Research Center (NSRRC). Data were collected in fluorescence mode using a Lytle detector, while the corresponding reference samples were collected in transmission mode. Samples were ground and uniformly coated on a special adhesive tape. The as-obtained XAFS data were processed in Athena (version 0.9.26) for background, pre-edge line, and post-edge line calibrations. Fourier transform fitting was then conducted in Artemis (version 0.9.26). The $k_3$ weighting, $k$ range of 1–6 Å$^{-1}$, and $R$ range of 1–4 Å were used for the fitting. The four parameters, namely, coordination number, bond length, Debye–Waller factor, and $E_0$ shift (CN, $R$, $\sigma^2$, and $\Delta E_0$), were fitted without any being fixed, constrained, or correlated. For wavelet transform analysis, $\chi(k)$ exported from Athena was imported into the Hama Fortran code. The parameters were as follows: $R$ range, 1–4 Å; $k$ range, 0–6 Å$^{-1}$; and $k$ weight, 2; the Morlet function with $\kappa = 10$ and $\sigma = 1$ was used as the mother wavelet to provide the overall distribution.

### $NH_3$-SCR activity measurements

The SCR reaction was evaluated in a fixed-bed reactor. The samples (0.3 g) were placed in reaction tubes, which were then placed in simulated flue gas for 2 h. The gas mixture contained NO (300 ppm), $NH_3$ (300 ppm), and $O_2$ (3%), with $N_2$ as the balancing gas. The gas hourly space velocity was ~30 000 h$^{-1}$. The catalytic activity was determined by analyzing the inlet and outlet gases using a flue gas analyzer (MultiGas 6030, MKS) at temperatures between 100 and 400 °C. At each temperature (100, 150, 200, 250, 300, 350, and 400 °C), the catalyst activity was determined after a reaction time of 1 h. The $NO_x$ conversion and $N_2$ selectivity were calculated as follows:

$$NO_x \text{ conversion} = [([NO_x]_{in} - [NO_x]_{out})/[NO_x]_{in}] \times 100\% \quad (3)$$

$$N_2 \text{ selectivity} = \left(1 - \frac{2[N_2O]_{out}}{[NO_x]_{in} + [NH_3]_{in} - [NO_x]_{out} - [NH_3]_{out}}\right) \times 100\% \quad (4)$$

where $NO_x$ is the sum of the NO and $NO_2$ concentrations, $[NO_x]_{out}$ is the outlet concentration of $NO_x$, $[NO_x]_{in}$ is the inlet concentration of $NO_x$, $[NH_3]_{out}$ is the outlet concentration of $NH_3$, $[NH_3]_{in}$ is the inlet concentration of $NH_3$, and $[N_2O]_{out}$ is the outlet concentration of $N_2O$.

For $H_2O$ and combined $SO_2$ + $H_2O$ resistance experiments, the SCR reaction was allowed to stabilize for 200 h at 350 °C with only 300 ppm NO + 3% $O_2$ + 300 ppm $NH_3$ blew in, generating steady-state conditions prior to introducing 8% $H_2O$ for 40 h and a 500 ppm $SO_2$ + 8% $H_2O$ combination for 340 h at 350 °C into the flue gas, respectively. Finally, $SO_2$ and $H_2O$ were successively cut off.

### DFT calculations

The Vienna *ab initio* package (VASP) was used to perform all density functional theory (DFT) calculations within the generalized gradient approximation (GGA) using the PBE formulation. The spin-polarization was considered in all computations. The projected augmented wave (PAW) potentials were selected to describe the ionic cores and account for valence electrons using a plane wave basis set with a kinetic energy cutoff of 500 eV. Partial occupancies of the Kohn–Sham orbitals were allowed using the Gaussian smearing method and a width of 0.05 eV. The electronic energy was considered self-consistent when the energy change was smaller than $10^{-5}$ eV. A geometry optimization was considered convergent when the force change was smaller than 0.01 eV Å$^{-1}$. On-site corrections (DFT+$U$) were applied to the 3d electrons of Ti atoms ($U_{eff}$ = 4.5 eV) using the approach of Dudarev *et al.*

The equilibrium lattice constants of the anatase $TiO_2$ unit cell were optimized to $a = b = 3.858$ Å, $c = 9.652$ Å using a 10 × 10 × 4 Monkhorst-Pack $k$-point grid for Brillouin zone sampling. These constants were then used to construct a $TiO_2(101)$ surface model with $p(1 \times 3)$ periodicity in the $x$ and $y$ directions and two stoichiometric layers in the $z$ direction with a vacuum depth of 15 Å to separate the surface slab from its periodic duplicates. This $TiO_2(101)$ surface model contained 24 Ti and 48 O atoms. The $TiO_2(101)$ surface with one oxygen vacancy was used to represent the hydrogenated $TiO_2$ (H-$TiO_{2-x}$). The N-doped hydrogenated $TiO_2$ (N-H-$TiO_{2-x}$) was simulated by using one N atom to replace the surface O atoms in $TiO_2(101)$. During structural optimization, a (2 × 2 × 1) $k$-point grid in the Brillouin zone was used for $k$-point sampling and the bottom stoichiometric layer was fixed, while the remaining atoms were allowed to fully relax.

The adsorption energy ($E_{ads}$) of adsorbate $A$ was defined as follows:

$$\Delta E_{ads} = E_{A/surf} - E_{surf} - E_{A(g)} \quad (5)$$

where $E_{A/surf}$, $E_{surf}$, and $E_{A(g)}$ are the energies of adsorbate $A$ adsorbed on the surface, the surface, and isolated molecule $A$. The isolated molecule was in a cubic periodic box with a side length of 20 Å, which was investigated by using a 1 × 1 × 1 Monkhorst-Pack $k$-point grid for Brillouin zone sampling.

## Conclusions

This work shows that N-H-$TiO_{2-x}$ constructed in conjunction with lattice defect engineering exhibited good $NH_3$-SCR performance. The denitrification efficiency of N-H-$TiO_{2-x}$ was greater than 90% at 300–400 °C. More importantly, this catalyst exhibited long-term stability, resistance to $H_2O$ and $SO_2$ and good poisoning tolerance. The results of this study confirmed that the *in situ* N-doping on oxygen vacancies in hydrogenated $TiO_{2-x}$ is the key step. The DFT calculations combined with the DRIFT spectra data demonstrate that the N-dopant acts as the catalytic active site for the $NH_3$-SCR denitrification process *via* the Eley–Rideal mechanism. The introduction of nonmetal

active sites greatly reduces the impact of toxic substances. This is because precious/transition metals are no longer required to act as active components. As such, the poisoning of precious/transition metals would be mitigated, while the expense of the catalysts can be greatly reduced. We anticipate that this research will assist in the future design of anti-poisoning catalysts with non-metal active sites through lattice defect engineering, which can be used in wide industrial catalysis applications.

## Author contributions

G. L. carried out all the relevant experiments, data analysis and wrote the first draft of the manuscript. B. D. W. led the research program and supervised this project. Y. J. X. provided suggestions for the project development. B. D. W., Y. W., Y. J. X. and C. P. advised and revised the manuscript. J. J. W. and Y. W. performed all the DFT calculations and analyzed the catalytic mechanisms. Y. L. L. and J. Y. C. did the *in situ* XPS experiments of hydrogenation of $TiO_{2-x}$. Z. H. H. did the EELS-STEM measurements. H. W. did some catalyst characterization measurements. H. Y. W. drew some figures. S. P. P., Z. R. M., J. M. and J. L. Z. did some $NH_3$-SCR measurements.

## Conflicts of interest

There are no conflicts to declare.

## Acknowledgements

We gratefully acknowledge W. F. Tu for the assistance during the *in situ* XPS experiments and data analysis. The *in situ* XPS experiments were performed at the School of Chemical Engineering and Energy, Zhengzhou University, China. This work was supported by the National Key Research and Development Program of China (grant no. 2019YFC1907500) and by the National Energy Group Project (grant no. ST930021011C and no. ST930022006C). This research was undertaken on the supercomputers in the National Computational Infrastructure (NCI) in Canberra, Australia, which is supported by the Australian Commonwealth Government and the Pawsey Supercomputing Centre in Perth with funding from the Australian Government and the Government of Western Australia.

## Notes and references

1 Catalyst Deactivation, in *Advances in Chemistry*, ed. J. B. Butt, American Chemical Society, Washington, DC, 1972, vol. 109, pp. 259–518.
2 Y. Peng, J. H. Li, W. Z. Si, J. M. Luo, Y. Wang, J. Fu, X. Li, J. Crittenden and J. M. Hao, *Appl. Catal., B*, 2015, **168–169**, 195–202.
3 Z. W. Huang, H. Li, J. Y. Gao, X. Gu, L. Zheng, P. P. Hu, Y. Xin, J. X. Chen, Y. X. Chen, Z. L. Zhang, J. M. Chen and X. F. Tang, *Environ. Sci. Technol.*, 2015, **49**, 14460–14465.
4 F. Tang, B. Xu, H. Shi, J. Qiu and Y. Fan, *Appl. Catal., B*, 2010, **94**, 71–76.
5 J. X. Liu, H. F. Cheng, H. L. Zheng, L. Zhang, B. Liu, W. Y. Song, J. Liu, W. S. Zhu, H. M. Li and Z. Zhao, *ACS Catal.*, 2021, **11**(24), 14727–14739.
6 Z. Chen, C. Bian, Y. B. Guo, L. Pang and T. Li, *ACS Catal.*, 2021, **11**(21), 12963–12976.
7 C. Xie, D. F. Yan, H. Li, S. Q. Du, W. Chen, Y. Y. Wang, Y. Q. Zou, R. Chen and S. Y. Wang, *ACS Catal.*, 2020, **10**, 11082–11098.
8 C. M. Yang, Y. X. Lu, L. Zhang, Z. J. Kong, T. Y. Yang, L. Tao, Y. Q. Zou and S. Y. Wang, *Small Struct.*, 2021, **2100058**, 1–25.
9 Y. Q. Zhang, L. Tao, C. Xie, D. D. Wang, Y. Q. Zou, R. Chen, Y. Y. Wang, C. K. Jia and S. Y. Wang, *Adv. Mater.*, 2020, **1905923**, 1–22.
10 X. B. Chen, L. Liu, P. Y. Yu and S. S. Mao, *Science*, 2011, **331**, 746–750.
11 Y. Liu, L. H. Tian, X. Y. Tan, X. Li and X. B. Chen, *Sci. Bull.*, 2017, **62**, 431–441.
12 V. A. Glezakou and R. Rousseau, *Nat. Mater.*, 2018, **17**, 856–857.
13 S. G. Ullattil, S. B. Narendranath, S. C. Pillai and P. Periyat, *Chem. Eng. J.*, 2018, **343**, 708–736.
14 T. S. Rajaraman, S. P. Parikh and V. G. Gandhi, *Chem. Eng. J.*, 2020, **389**, 123918.
15 H. Y. Hu, Y. Lin and Y. H. Hu, *Phys. Lett. A*, 2019, **383**, 2978–2982.
16 S. X. Liu, S. Yuan, Q. Zhang, B. Xu, C. Wang, Z. Ming and O. Teruhisa, *J. Catal.*, 2018, **366**, 282–288.
17 C. Y. Han, S. L. Zhang, L. N. Guo, Y. Q. Zeng, X. H. Li, Z. C. Shi, Y. Zhang, B. Q. Zhang and Q. Zhong, *Chem. Eng. Res. Des.*, 2018, **136**, 219–229.
18 Y. Q. Zeng, Y. N. Wang, S. L. Zhang and Q. Zhong, *Phys. Chem. Chem. Phys.*, 2018, **20**, 22744–22752.
19 H. Q. Tan, Z. Zhao, M. Niu, C. Y. Mao, D. P. Cao, D. J. Cheng, P. Y. Feng and Z. C. Sun, *Nanoscale*, 2014, **6**, 10216–10223.
20 Y. Lu, W. J. Yin, K. L. Peng, K. Wang, Q. Hu, A. Selloni, F. R. Chen, L. M. Liu and M. L. Sui, *Nat. Commun.*, 2018, **9**, 2752.
21 K. Lan, R. C. Wang, Q. L. Wei, Y. X. Wang, A. Hong, P. Y. Feng and D. Y. Zhao, *Angew. Chem., Int. Ed.*, 2020, **59**, 17676–17683.
22 T. Q. Lin, C. Y. Yang, Z. Wang, H. Yin, X. J. Lü, F. Q. Huang, J. H. Lin, X. M. Xie and M. H. Jiang, *Energ. Environ. Sci.*, 2014, **7**, 967.
23 P. Pichat, *Cataly. Today*, 2020, **340**, 26–33.
24 L. Pan, M. H. Ai, C. Y. Huang, L. Yin, X. Liu, R. R. Zhang, S. B. Wang, Z. Jiang, X. W. Zhang, J. J. Zou and W. B. Mi, *Nat. Commun.*, 2020, **11**, 418.
25 F. Li, W. H. Huang and X. Q. Gong, *Chin. Chem. Lett.*, 2018, **29**, 765–768.
26 A. Naldoni, M. Allieta, S. Santangelo, M. Marelli, F. Fabbri, S. Cappelli, C. L. Bianchi, R. Psaro and V. D. Santo, *J. Am. Chem. Soc.*, 2012, **134**, 7600–7603.

27 M. I. Nandasiri, V. Shutthanandan, S. Manandhar, A. M. Schwarz, L. Oxenford, J. V. Kennedy, S. Thevuthasan and M. A. Henderson, *J. Phys. Chem. Lett.*, 2015, **6**, 4627–4632.
28 R. Schaub, E. Wahlström, A. Rønnau, E. Lægsgaard, I. Stensgaard and F. Besenbacher, *Science*, 2003, **299**, 377–379.
29 D. N. Pei, L. Gong, A. Y. Zhang, X. Zhang, J. J. Chen, Y. Mu and H. Q. Yu, *Nat. Commun.*, 2015, **6**, 8696.
30 D. Pietrogiacomi, D. Sannino, A. Magliano, P. Ciambelli, S. Tuti and V. Indovina, *Appl. Catal., B*, 2002, **36**, 217–230.
31 L. Ma, J. Li, R. Ke and L. Fu, *J. Phys. Chem. C*, 2011, **115**, 7603–7612.
32 U.S. Department of Commerce. The National Institute of Standards and Technology (NIST) X-ray Photoelectron Spectroscopy (XPS) Database Main Search Menu (2003); **https://www.nist.gov/**.
33 N. Y. Topsoe, *Science*, 1994, **265**, 1217–1219.
34 N. Y. Topsoe, J. A. Dumesic and H. Topsoe, *J. Catal.*, 1995, **151**, 241–252.
35 G. Z. He, Z. H. Lian, Y. B. Yu, Y. Yang, K. Liu, X. Y. Shi, Z. D. Yan, W. P. Shan and H. He, *Sci. Adv.*, 2018, **4**, eaau4637.
36 S. J. Yang, Y. F. Guo, H. Z. Chang, L. Ma, Y. Peng, Z. Qu, N. Q. Yan, C. Z. Wang and J. H. Li, *Appl. Catal., B*, 2013, **136–137**, 19–28.
37 G. Kresse and J. Furthmüller, *Comput. Mater. Sci.*, 1996, **6**, 15–50.
38 G. Kresse and J. Furthmüller, *Phys. Rev. B: Condens. Matter Mater. Phys.*, 1996, **54**, 11169–11186.
39 J. P. Perdew, K. Burke and M. Ernzerhof, *Phys. Rev. Lett.*, 1996, **77**, 3865–3868.
40 R. T. Wilburn and T. L. Wright, *PowerPlant Chem.*, 2004, **6**, 295–314.
41 J. M. Burke and K. L. Johnson, *Environmental Protection Agency*, Washington, DC, United States, 1982.